Journal of Colloid and Interface Science 628 (2022) 398–406

Contents lists available at ScienceDirect

Journal of Colloid and Interface Science

journal homepage: www.elsevier.com/locate/jcis

Structural engineering and electronic state tuning optimization of molybdenum-doped cobalt hydroxide nanosheet self-assembled hierarchical microtubules for efficient electrocatalytic oxygen evolution

Chao Wang [a], Wen Li [a], Andrey A. Kistanov [b], Harishchandra Singh [b], Yves Kayser [c], Wei Cao [b], Baoyou Geng [a,d,*]

[a] College of Chemistry and Materials Science, The Key Laboratory of Functional Molecular Solids, Ministry of Education, The Key Laboratory of Electrochemical Clean Energy of Anhui Higher Education Institutes, Anhui Provincial Engineering Laboratory for New-Energy Vehicle Battery Energy-Storage Materials, Anhui Normal University, Wuhu 241002, China
[b] Nano and Molecular Systems Research Unit, University of Oulu, FIN-90014, Finland
[c] Physikalisch-Technische Bundesanstalt, X-ray Spectrometry Abbestr. 2-12, 10587 Berlin, Germany
[d] Institute of Energy, Hefei Comprehensive National Science Center, Hefei 230031, China

HIGHLIGHTS

- Mo-doped cobalt hydroxide nanosheet hierarchical microtubules are fabricated using MoO_3 nanorods as sacrificial templates.
- X-ray-based spectroscopic tests reveal that Mo (VI) with tetrahedral coordination intercalate into the interlayer of cobalt hydroxide.
- Under alkaline condition, the OER overpotential is 288 mV at a current density of 10 mA cm^{-2}.

GRAPHICAL ABSTRACT

Self-assembled cobalt-molybdenum layered double hydroxide hierarchical microtubes are synthesized based on a structural engineering and electronic state tuning, it has excellent performance for OER.

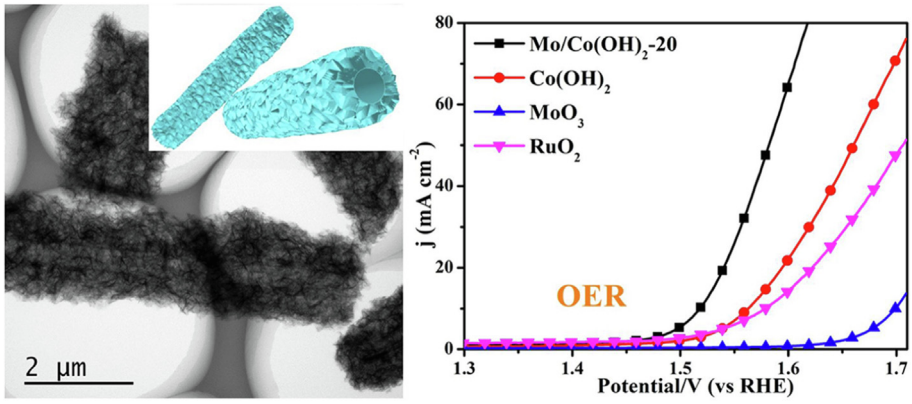

ARTICLE INFO

Article history:
Received 9 July 2022
Revised 10 August 2022
Accepted 11 August 2022
Available online 17 August 2022

Keywords:
Cobalt-based hydroxide
Structural engineering
Self-assembled

ABSTRACT

Cobalt-based hydroxide are ideal candidates for the oxygen evolution reaction. Herein, we use molybdenum oxide nanorods as sacrificial templates to construct a self-supporting molybdenum-doped cobalt hydroxide nanosheet hierarchical microtubule structure based on a structural engineering strategy to improve the active area of the catalyst. X-ray-based spectroscopic tests revealed that Mo (VI) with tetrahedral coordination intercalated into the interlayer of cobalt hydroxide, promoting interlayer separation. At the same time, Mo is connected with Co through oxygen bonds, which promotes the transfer of Co charges to Mo and reduces the electron cloud density of Co ions. In 1 M KOH, optimized molybdenum-doped cobalt hydroxide nanosheet microtubules only needs an overpotential of 288 mV to drive a current density of 10 mA cm^{-2}, which is significantly better than that of pure $Co(OH)_2$ nanosheets and RuO_2. Structural engineering and electronic state regulation can effectively improve the oxygen evolution

* Corresponding author at: College of Chemistry and Materials Science, The Key Laboratory of Functional Molecular Solids, Ministry of Education, The Key Laboratory of Electrochemical Clean Energy of Anhui Higher Education Institutes, Anhui Provincial Engineering Laboratory for New-Energy Vehicle Battery Energy-Storage Materials, Anhui Normal University, Wuhu 241002, China.
E-mail address: bygeng@mail.ahnu.edu.cn (B. Geng).

https://doi.org/10.1016/j.jcis.2022.08.069

Oxygen evolution reaction

activity of cobalt-based hydroxide, which provides a design idea for the development of efficient oxygen evolution catalysts.

1. Introduction

The oxygen evolution reaction (OER) is an essential and critical half-reaction in various renewable energy applications, such as water splitting, renewable fuel cells, and metal-air batteries [1–3]. However, the reaction kinetics of OER is sluggish, and there is an urgent need to develop cheap OER catalysts to replace scarce and expensive Ir, Ru-based materials [4–6]. In recent years, abundant and inexpensive transition metal-based materials have become the focus of OER catalyst research [7,8]. Among them, cobalt-based hydroxide have received extensive attention due to the presence of unsaturated CoO_{6-x} octahedra with high catalytic activity [9–12]. Its unique layered structure facilitates the exposure of active sites and increases the electrochemical active area [13]. However, during use, the inevitable stacking of nanosheets reduces the exposure of active sites and limits the catalytic activity [14]. To avoid the stacking of nanosheets, the researchers grew nanosheet arrays on substrates such as nickel foam, copper foam, and carbon cloth [15–19]. However, the catalytic activity of the matrix itself is not good, and the mass proportion of the material is relatively high, which reduces the mass activity of the material. Constructing a self-assembled 3D structure of active nanosheets can effectively support and separate the nanosheets, increase the exposed area of the nanosheets, and improve the structural stability [20,21]. The rational design of the material structure is expected to obtain highly active cobalt-based catalysts.

Introducing other metal elements, using intermetallic interactions to adjust the Co-3d orbital electronic structure, and optimizing the adsorption energy for OER reaction intermediates is a common strategy to improve the activity of cobalt-based catalysts [22,23]. Transition metals with the same period as Co, such as Fe, Ni, etc., are widely used to develop cobalt-based catalysts [24–27]. However, their similar structure limits the space for electronic structure regulation. It has been reported that $Co^{2+}/^{3+}$ transition occurs in cobalt-based materials during the OER process, while high-valent cobalt exhibits high activity [28]. Zhang et al. showed that doping metals with high valence charges can tune 3d metals and reduce the energy of valence-charge transitions, resulting in better catalytic OER performance [29]. Due to the outstanding electron-withdrawing ability of Mo, the electrons of the 3d metal are transferred to Mo (VI) under the oxidation potential, which is beneficial for the 3d metal to maintain its high valence state [30,31]. Therefore, the preparation of molybdenum-doped cobalt hydroxide is expected to yield high-performance OER catalysts.

Here, we successfully constructed a cobalt-molybdenum nanosheet self-assembled hierarchical microtubule structure ($Mo/Co(OH)_2$ HMT) using molybdenum oxide nanorods as a sacrificial template, which effectively improved the dispersion of the nanosheets and increased the active area of the material. X-ray based spectroscopic measurements show that Mo (VI) with tetrahedral coordination intercalated into the interlayer of cobalt hydroxide, promoting interlayer separation. Meanwhile, Mo induces Co charge transfer through oxygen bonds, increasing the valence state of Co. In 1 M KOH, the OER overpotential required for $Mo/Co(OH)_2$ HMT to drive a current density of 10 mA cm^{-2} is only 288 mV, which is significantly better than that of $Co(OH)_2$ nanosheets (333 mV) and RuO_2 (349 mV). Through structural engineering and electronic state regulation, the OER activity of cobalt-based hydroxides has been significantly improved, providing a research idea for the development of efficient OER catalysts.

2. Experimental

2.1. Materials preparation and characterization

$(NH_4)_6Mo_7O_{24}·4H_2O$ (AR), $Co(NO_3)_2·6H_2O$ (AR), polyvinylpyrrolidone (PVP, Mw = 40000), MoO_3 (≤10 μm), N, *N*-dimethylformamide (DMF, AR) and KOH (99.999%) were provided by Aladdin Industrial Corporation. HNO_3 (AR), $Fe(NO_3)_3·9H_2O$ (AR), and $Ni(NO_3)_2·6H_2O$ (AR) were purchased from Sinopharm Chemical Reagent Co. Sodium borohydride ($NaBH_4$, AR) was bought from Jiuding Chemical Reagent Co. All materials used directly without further purity. Deionized water (18.25 MΩ·cm resistivity) was obtained by using PSDK water purification system.

2.2. Synthesis of MoO_3 nanorods (NRs)

1.05 g $(NH_4)_6Mo_7O_{24}·4H_2O$ was dissolved in a mixed solution of 25 mL H_2O and 5 mL HNO_3. After stirring for 30 min, the solution was poured into a 50 mL autoclave and incubated at 200 °C for 20 h. After naturally cooling to room temperature, the product was collected through centrifuging and washing with deionized water and ethanol 3 times. Finally, the product was dried in a vacuum oven at 60 °C for 12 h.

2.3. Synthesis of $Mo/Co(OH)_2$ hierarchical microtubes (HMTs)

0.1 g MoO_3 nanorods, a certain volume of cobalt nitrate aqueous solution (0.1 M) (V = 10, 15, 20, 30 mL) and the corresponding mass of PVP (m = 0.1, 0.15, 0.2, 0.3 g) were dispersed in the aqueous solution to ensure that the total volume of the solution was 60 mL. Then, under stirring conditions, 10 mL of the corresponding concentration of sodium borohydride aqueous solution (0.01, 0.015, 0.02, 0.03 g/mL) was slowly added into above solution and all drops within 1 h. The above solution was further stirred for 10 h to obtain $Mo/Co(OH)_2$ HMT. The products were collected by centrifugation, washed three times with water and ethanol, and dried under vacuum at 60 °C for 12 h. According to the different volume of cobalt nitrate solution, the samples are marked as $Mo/Co(OH)_2$-10; $Mo/Co(OH)_2$-15; $Mo/Co(OH)_2$-20; $Mo/Co(OH)_2$-30.

2.4. Synthesis of $Co(OH)_2$ nanosheets (NSs)

0.2 g of PVP and 1 mmol of $Co(NO_3)_2·6H_2O$ were added to 60 mL of deionized water, stirred and dispersed uniformly. With stirring, 10 mL of sodium borohydride aqueous solution (0.02 g/mL) was added dropwise to the above solution. After continue stirring for 10 h, the product was collected by centrifugation and washed with water and ethanol three times, and dried in vacuum at 60 °C for 12 h.

2.5. Synthesis of MoO_3 NPs-$Co(OH)_2$

The preparation process of MoO_3 NPs-$Co(OH)_2$ is similar to $Mo/Co(OH)_2$-20, except that MoO_3 nanorods are replaced with MoO_3 nanoparticles. 0.1 g of commercial MoO_3 nanoparticles in was dispersed in 40 mL water, and then 20 mL of cobalt nitrate aqueous solution (0.1 M) and 0.2 g of PVP were added into above solution under stirring. Next, 10 mL of sodium borohydride aqueous solution (0.02 g/mL) was added dropwise to the above solution. After continue stirring for 10 h, the product was collected by centrifuga-

tion, washed with water and ethanol three times, and dried in vacuum at 60 °C for 12 h.

2.6. Material characterizations

The morphologies of the samples were characterized by scanning electron microscopy (SEM, Hitachi S-4800) and transmission electron microscopy (TEM, Hitachi, HT-7700). The morphology and high-angle annular dark field (HAADF) image of Mo/Co $(OH)_2$-20 were tested by high-resolution transmission electron microscope (HRTEM, FEI Tecnai F30). In order to study the element distribution of Mo/Co$(OH)_2$-20 and the change of element distribution during the material preparation process, the element composition was tested (EDAX Genesis). X-ray powder diffraction (XRD, Bruker AXS, D8 Advance) characterizations were carried out by Cu Kα radiation. The content of Mo and Co in Mo/Co$(OH)_2$-20 was tested by inductively coupled plasma emission spectrometry (ICP-OES, PerkinElmer, Optima 8000). The surface composition and chemical valence of the samples were analyzed by X-ray photoelectron spectroscopy (XPS, Thermo ESCALAB 250XI). The specific surface area and pore size distribution of samples were tested by N_2 adsorption/desorption (Micromeritics ASAP 2020). The catalytic performance of the samples was evaluated by electrochemical workstation (CHI 760E, China).

2.7. X-ray absorption measurements

The X-ray absorption near edge structure (XANES) measurements at the Mo $L_{3\text{-}2}$-edges and at the Co K-edge were recorded in fluorescence mode at the four-crystal monochromator (FCM) beamline [32] of the Physikalisch-Technische Bundesanstalt (PTB) at the BESSY II electron storage ring [33]. At this bending magnet beamline four Si (1 1 1) crystals were used to monochromatize the radiation and the design of the unit allows for a fixed beam position [34]. The use of four monochromator crystals allows for the provision of X-ray radiation with a high spectral resolving power of 10^4 while the uncertainty of the energy scale of the FCM is 0.5 eV.

The experiments were carried out using an in-house developed ultrahigh vacuum chamber [34]. The samples were excited using an incident angle of 45° and the X-ray fluorescence radiation was detected using a calibrated silicon drift detector (SDD) positioned at a detection angle of 45°. Thus, the SDD is oriented perpendicular to the incident radiation and since it is positioned within the polarization plane of the synchrotron radiation used, scattering contributions in the detected spectra are minimized. For normalization purposes, the incident photon energy dependent incident flux of the beamline was measured beforehand using a thin photodiode in transmission. The incident photon energy was varied in energy steps of 0.3 eV from 2505 to 2565 eV for the measurements at the Mo L_3 ionization threshold and the detector lifetime was varied between 5 s and 25 s, depending on the sample. For the measurements around the Co K ionization threshold, 0.5 eV energy steps were used in the vicinity of the ioniztation threshold (7700 eV to 7750 eV). Depending on the sample detection times between 10 s and 30 s were used. The measured spectra were deconvoluted using the detector response functions for the different fluorescence lines detected and other relevant background contributions in order to derive the count rates of the Mo L_3, and the Co K fluorescence lines, respectively [35].

2.8. Electrocatalytic measurements

Preparation of working electrode: 2 mg catalyst and 1 mg carbon black (Vulcan XC-72) were uniformly dispersed in 650 μL deionized water, 330 μL DMF and 20 μL Nafion solution (5%). Ultrasonic dispersion for 30 min to obtain a uniform catalyst ink. 7 μL of ink was dropped on the surface of a glassy carbon electrode (d = 3 mm) polished with alumina powder and dried naturally to obtain a working electrode with a catalyst loading of 0.2 mg cm^{-2}. The electrochemical test was performed by using the CHI 760E electrochemical workstation (Shanghai Chenhua, three-electrode system). The catalyst-coated glassy carbon electrode was used as the working electrode, and saturated Ag/AgCl electrode was the reference electrode and a salt bridge was added. The graphite rod was used as a counter electrode. Before the test, oxygen must be injected for a period of time to ensure that the electrolyte is saturated with oxygen. The potentials in this work were converted to RHE according to $E_{RHE} = E_{Ag/AgCl} + 0.197 + 0.059 \times pH$ (1 M KOH, pH ≈ 13.8). The linear sweep voltammetry curve (LSV) of OER activities were performed in O_2-saturated 1 M KOH with a scan rate of 10 mV s^{-1} at room temperature. The cyclic voltammetry (CV) curve was tested at different scanning speeds (20 to 120 mV s^{-1}) to obtain the double-layer capacitance (Cdl) of the catalyst to compare the electrochemically surface area of the catalyst. In order to test the stability of the material, at room temperature, under the condition of 1 M KOH saturated with O_2, test the chronopotentiometry curve when the current density is 10 mA cm^{-2}. In this study, all potentials were not compensated for iR. The overpotential (η) is calculated according to the following formula: $\eta = E_{RHE} - 1.23$ V. Mass activity (j_m) calculation method: j_m = j/m, m is the catalyst loading on the working electrode (mg), j is the current value (mA) measured at an overpotential (η) of 350 mV.

3. Results and discussion

3.1. Synthesis and materials characterization

We use PVP as a template agent and sodium borohydride as a reducing agent, and gradually grow cobalt hydroxide nanosheets through the reduction and reoxidation of cobalt ions [36]. However, the as-prepared nanosheets are curled and packed (Fig. S1), which is not conducive to the exposure of active sites, limiting the performance of the catalyst. To improve the dispersibility of nanosheets, we introduced MoO_3 nanorods as sacrificial templates to obtain hierarchical microtubular structures composed of molybdenum-doped cobalt hydroxide nanosheets (Mo/Co$(OH)_2$ HMTs). Fig. 1a-h demonstrate gradual loading of nanosheets on the microtubes by controlling the ratio of cobalt nitrate to molybdenum oxide. When the amount of cobalt nitrate solution increased from 10 mL to 30 mL, the density of nanosheets on the sample tube wall gradually increased, and the products were marked as Mo/Co$(OH)_2$-10, Mo/Co$(OH)_2$-15, Mo/Co$(OH)_2$-20, Mo/Co$(OH)_2$-30, respectively. In order to compare the surface area of the sample, we tested the N_2 adsorption-desorption isotherm of the sample (Fig. S4a). The isotherm of Mo/Co$(OH)_2$ HMTs is type IV, with H3 hysteresis loop [37]. As shown in Fig. S4a, the Brunauer-Emmett-Teller surface area (S_{BET}) of Mo/Co$(OH)_2$ HMTs is significantly larger than that of cobalt hydroxide nanosheets and molybdenum oxide nanorods. This shows that the construction of the composite structure effectively increases the surface area of the material. As the amount of cobalt nitrate increases, the S_{BET} of the material first increases and then decreases. This may be because increasing the loading of nanosheets helps to increase the surface area of the material. However, too high load will cause the nanosheets on the microtubes to overlap. When the amount of cobalt nitrate solution was 20 mL, the specific surface area of the material reached 277.5 m^2 g^{-1}, which was the largest among the prepared samples. From the pore size distribution diagram (Fig. S4b), Mo/Co$(OH)_2$ HMTs significantly increased the

volume of mesopores. The increase in pore volume is conducive to electrolyte penetration and gas diffusion and is benefit for the progress of electrocatalytic reactions. Since Mo/$Co(OH)_2$-20 has the highest surface area, we conducted further research on it.

As shown in Fig. 1i, an obvious tubular structure can be seen in the high-magnification TEM image with a tube diameter of about 350 nm. The partially enlarged TEM image (Fig. 1j) shows that the nanosheets on the microtubes are very thin. The HRTEM images and selected area electron diffraction (SAED) patterns of $Co(OH)_2$ NS and Mo/$Co(OH)_2$-20 are shown in Fig. 5S. It can be found that both $Co(OH)_2$ NS and Mo/$Co(OH)_2$-20 exhibit a certain degree of crystallinity (Fig. S5b, S5e), and the difference of interplanar spacings is not obvious. However, the crystal planes after doping with Mo are clearly more chaotic than before, indicating that Mo doping has a certain influence on its structure. Fig. S5c and S5f reveal that the diffraction rings of $Co(OH)_2$ NS and Mo/$Co(OH)_2$-20 are similar, indicating that the structure does not change much, which is consistent with the lower doping amount. In addition, there are diffraction spots in the diffraction ring of $Co(OH)_2$ NS, indicating that the grain size in $Co(OH)_2$ NS is larger, which is consistent with the HRTEM results. Element mappings show that the Mo, Co, and O in the sample are uniformly distributed (Fig. 1k-n).

To explore the growth mechanism of Mo/$Co(OH)_2$, we selected products from different reaction time stages for HAADF and elemental mapping characterization. Fig. 2 shows the morphology and composition evolution of the product starting from the addition of sodium borohydride. We found that the MoO_3 nanorods gradually thinned with increasing reaction time, which was the result of the continuous decomposition of the nanorods due to the reduction of molybdenum oxide by sodium borohydride. Meanwhile, PVP induces cobalt ions to form $Co(OH)_2$ nanosheets, which grow around the nanorods and capture the molybdenum released by the decomposition of the nanorods. The XRD diffraction peaks of MoO_3 after the reaction for 10 min and 30 min gradually disappeared (Fig. S6), which proved the etching effect of sodium borohydride on MoO_3. After 65 min of reaction, the MoO_3 nanorods disappeared completely. Cobalt and molybdenum are almost uniformly distributed in the nanorods. From 1.5 to 11 h, with the extension of the reaction time, the cobalt and molybdenum are completely uniformly dispersed, the diameter of the product tube becomes thicker, and the load of nanosheets

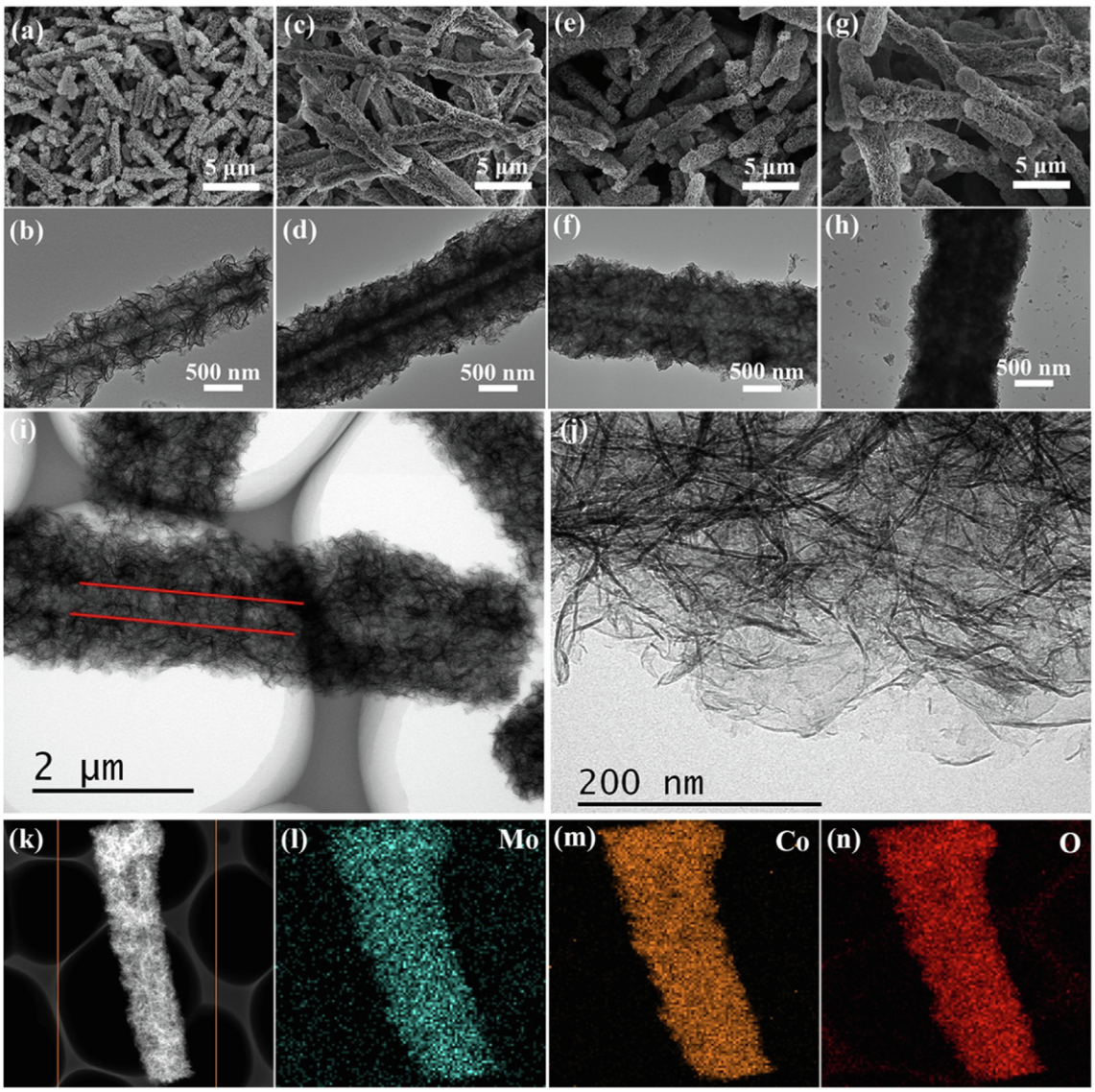

Fig. 1. Mo/$Co(OH)_2$ HMTs with different loadings of nanosheets: SEM and TEM images of Mo/$Co(OH)_2$-10 (a, b), Mo/$Co(OH)_2$-15 (c, d), Mo/$Co(OH)_2$-20 (e, f), Mo/$Co(OH)_2$-30 (g, h), respectively. (i, j) High-magnification TEM images of Mo/$Co(OH)_2$-20. (k-n) The HAADF image and corresponding element mappings of Mo/$Co(OH)_2$-20.

increases. During the entire reaction, the nanoparticles appeared and disappeared many times. This is because when there is more sodium borohydride in the solution, a large amount of metal is reduced to form nanoparticles.

We systematically performed investigations using different X-ray based techniques to determine structural and electronic structure properties of materials. In the XRD patterns (Fig. 3a), compared with $Co(OH)_2$ NSs, the peak of Mo/$Co(OH)_2$-20 at about 20° shifted to higher 2θ direction, while the other peaks changed less. This indicates that Mo doping leads to the structural change in the cobalt hydroxide. Two possibilities of Mo doping in cobalt hydroxide nanosheets have been speculated according to literature [38]. As shown in Fig. 3b, i) Mo can replace Co sites and exhibits similar octahedra like CoO_6 in layered hydroxide and ii) Mo can intercalate into cobalt hydroxide nanosheets.

The XPS spectrum uses the C 1s electron peak (BE = 284.8 eV) as a reference for spectral calibration. Fig. S7 shows the XPS total spectrum of Mo/$Co(OH)_2$-20, $Co(OH)_2$ NSs and MoO_3 NRs. The XPS test result shows that the atomic ratio of Mo: Co in Mo/Co $(OH)_2$-20 is 1:12. The ICP test shows that the Mo, Co content of Mo/$Co(OH)_2$-20 is 6.8 wt% and 48.6 wt%. The strong peaks at 780.8 and 796.7 eV in the Co 2p spectrum of $Co(OH)_2$ NSs correspond to Co $2p_{3/2}$ and $2p_{1/2}$ [39,40]. The binding energies of Co $2p_{3/2}$ (781.3 eV) and $2p_{1/2}$ (797.2 eV) increased by 0.5 eV after Mo doping. This may be due to the higher electronegativity of Mo than that of Co, resulting in a decrease in the electron cloud density of Co and an increase in the binding energy. The high-resolution XPS Mo 3d spectra (Fig. 3d) show that Mo $3d_{5/2}$ and $3d_{3/2}$ in Mo/$Co(OH)_2$-20 are located at 232.4 eV and 235.5 eV, respectively. The peak spacing of Mo $3d5_{/2}$ and $3d_{3/2}$ is 3.1 eV, which is consistent with that reported for Mo (VI) [41,42]. Compared with MoO_3 NRs, the binding energy of Mo 3d is reduced by 0.5 eV. The shift in binding energy of Mo 3d much lesser than the required reported shift for Mo (IV) and Mo (V) [43,44], indicating the existence of Mo (VI) in Mo/$Co(OH)_2$-20 but subjected to coordination changes. Observed binding energy shifts for Co and Mo in XPS data indicate the charge transfer from Co to Mo.

X-ray absorption spectroscopy was performed to probe the chemical environments of Co and Mo in $Co(OH)_2$, MoO_3, Mo/Co $(OH)_2$-20. In addition, in the preparation process of Mo/$Co(OH)_2$-20, the products obtained 20 min and 65 min after the addition of sodium borohydride were also tested. Fig. 3e and 3f show normalized X-ray absorption near-edge structure (XANES) recorded next to Co K- and Mo L_3- edges. The normalization was performed by using the pre-edge and post-edge regions where atom-liked transitions dominate. Three visible changes marked by P (pre-edge), E (edge) and W (white line) in Co K-edge XANES spectra correspond to structural polyhedral distortion, electron transfer and electronic structure variation, respectively [45,46]. Pre-edge commonly assigns to the dipole-forbidden 1s → 3d transition and strongly refers to the type of local coordination such as tetrahedral, octahedral etc [47]. A finite peak intensity can arise either from the Co 3d-4p hybridization or from Co 3d to ligand 2p mixing through distortion. As shown in Fig. S8, the strength of the pre-edge feature of Mo/$Co(OH)_2$-20 is slightly seems to be reduced compared with $Co(OH)_2$. The slight shift in energy of Mo/$Co(OH)_2$-20 spectrum with respect to $Co(OH)_2$ indicate the possible charge transfer, a result which is also matching with the XPS observation. In addition, the increase in the characteristic strength of the leading edge of the reaction intermediates, especially the products reacted for 65 min, indicates that the coordination structure of Co changes significantly during the material preparation. The white line feature shows different electronic density of states in these samples [48]. Compared with $Co(OH)_2$, after doping with Mo, the white line feature is slightly elevated, indicating that Co has more unoccupied density of states in the material.

Fig. 3f shows the edge step normalized XANES spectrum of the Mo L_3-edge. Mo L_3-edge XANES denotes transitions from 2p to unoccupied d-typed states. The bimodal structure of features A and B caused by crystal field splitting is clearly visible for all the measured samples. In the case of octahedral Mo (VI) (such as MoO_6 in MoO_3), the first peak (A) has greater intensity, while in the case of tetrahedral Mo (VI) (such as MoO_4^{2-}), the second peak (B) has greater intensity [49,50]. With the prolongation of the reaction time, the peak A weakened and the peak B enhanced, indicating that the coordination structure of Mo ions in the material was transformed from octahedral to tetrahedral. Furthermore, the splitting of Mo 4d in the octahedral environment is superior to that in the tetrahedral environment. The splitting peak spacings of MoO_3 and Mo/$Co(OH)_2$-20 are 2.8 eV and 2 eV, respectively. The narrowing of the peak spacing also indicates the transformation of the Mo coordination structure from octahedral to tetrahedral.

Based on X-ray studies, the possible charge transfer mechanism in Mo/$Co(OH)_2$-20 is shown in Fig. 3g. Mo exists in the form of tetrahedral-coordinated Mo (VI), which is connected to cobalt ions through oxygen bonds. The Mo ion transitions from octahedral to tetrahedral coordination, and the charge balance required for the transition is provided by cobalt ions, resulting in an elevated valence state of cobalt. Co ions in cobalt hydroxide exist in octahedral coordination structure, while Mo ions in Mo/$Co(OH)_2$-20 are tetrahedral coordination. This suggests that Mo ions intercalate into the cobalt hydroxide interlayer instead of replacing the Co sites. The intercalation of Mo ions promotes the separation between layers.

3.2. Electrochemical performance

To explore the effect of Mo doping and material structure on the catalytic performance, we tested the OER performance of the samples. Fig. S9 shows the optical pictures of the sample powder, catalyst ink, working electrodes and the test setup, respectively. The LSV curves in Fig. 4a show that that the MoO_3 nanorods have almost no OER performance. After being interacted with the cobalt hydroxide nanosheets, the catalytic performance is significantly improved, and both exceed the pure cobalt hydroxide nanosheets. Mo/$Co(OH)_2$-20 has the best catalytic performance. It only needs 288 mV overpotential (η) to drive 10 mA cm^{-2}, which is significantly better than $Co(OH)_2$ nanosheets (333 mV), and also better than commercial RuO_2 (349 mV). Fig. 4b and Table S2 show the overpotential and mass activity of the samples. The mass activity of Mo/$Co(OH)_2$-20 is 3.2 times that of $Co(OH)_2$. The Tafel slope of Mo/$Co(OH)_2$-20 has the smallest value of 69.7 mV/dec (Fig. 4c), indicating that the material has a higher reaction rate. Since the double-layer capacitance (Cdl) is proportional to the electrochemically active area of the material, we compared the active area by testing the Cdl of the materials [51,52]. The CV curves at different scan rates are shown in Fig. S10. Capacitive current is plotted against scan rate (Fig. 4d), with a slope twice that of Cdl. As shown in Fig. 4e, the highest capacitance value of Mo/$Co(OH)_2$-20 indicates that it has the largest electrochemical surface area. By comparing the electrochemical performance of the samples, it is not difficult to see that Mo/$Co(OH)_2$-20 has the best catalytic performance. In addition, the relationship between the capacitance of the sample is consistent with the results of S_{BET} and OER activity, indicating that the activity of the catalyst are improved by structural design and increasing the surface area of the material. Stability is also another important criterion for evaluating catalysts. The LSV curves of Mo/$Co(OH)_2$-20 in Fig. 4f almost overlap after 1000 cycles. Moreover, after the chronopotentiometry test (the inset in Fig. 4f), the potential did not increase significantly, indicating that Mo/$Co(OH)_2$-20 has good stability. The SEM and TEM characteriza-

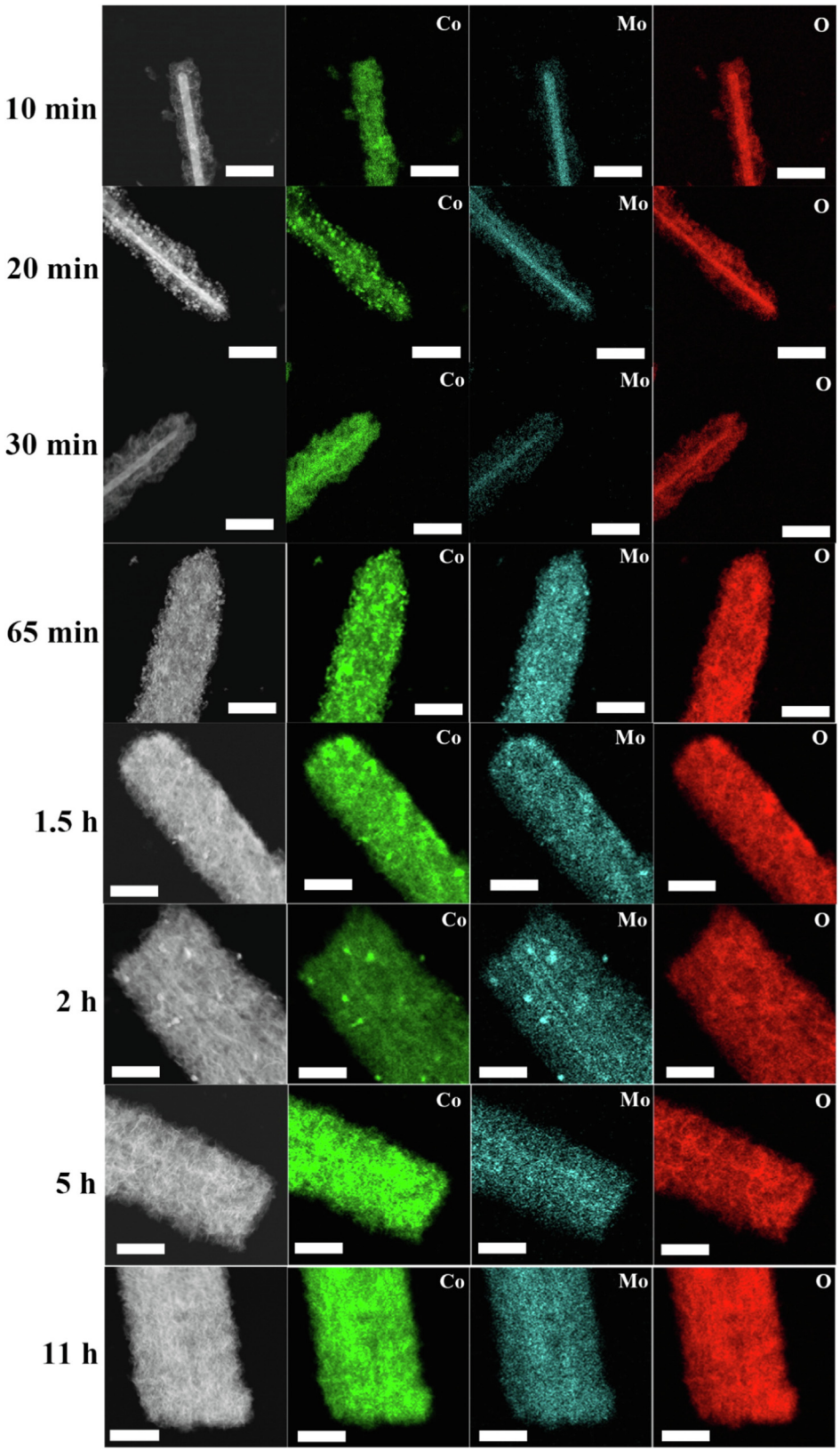

Fig. 2. HAADF images and corresponding Co, Mo, O mappings of products with different reaction times during the preparation of Mo/Co(OH)$_2$-20. (The scales are all 1 μm).

tions of the samples after the reaction showed that the structure of the material remained stable (Fig. S11).

In addition, we also used MoO_3 nanoparticles instead of nanorods, and other conditions were consistent with Mo/Co(OH)$_2$-20 to obtain MoO_3 NPs-Co(OH)$_2$. Since MoO_3 NPs have no regular morphology (Fig. S12a), the nanosheets cannot be induced to grow according to a certain rule, and the morphology of MoO_3NPs-Co(OH)$_2$ as stacked nanosheets (Fig. S12b-d). Energy dispersive spec-

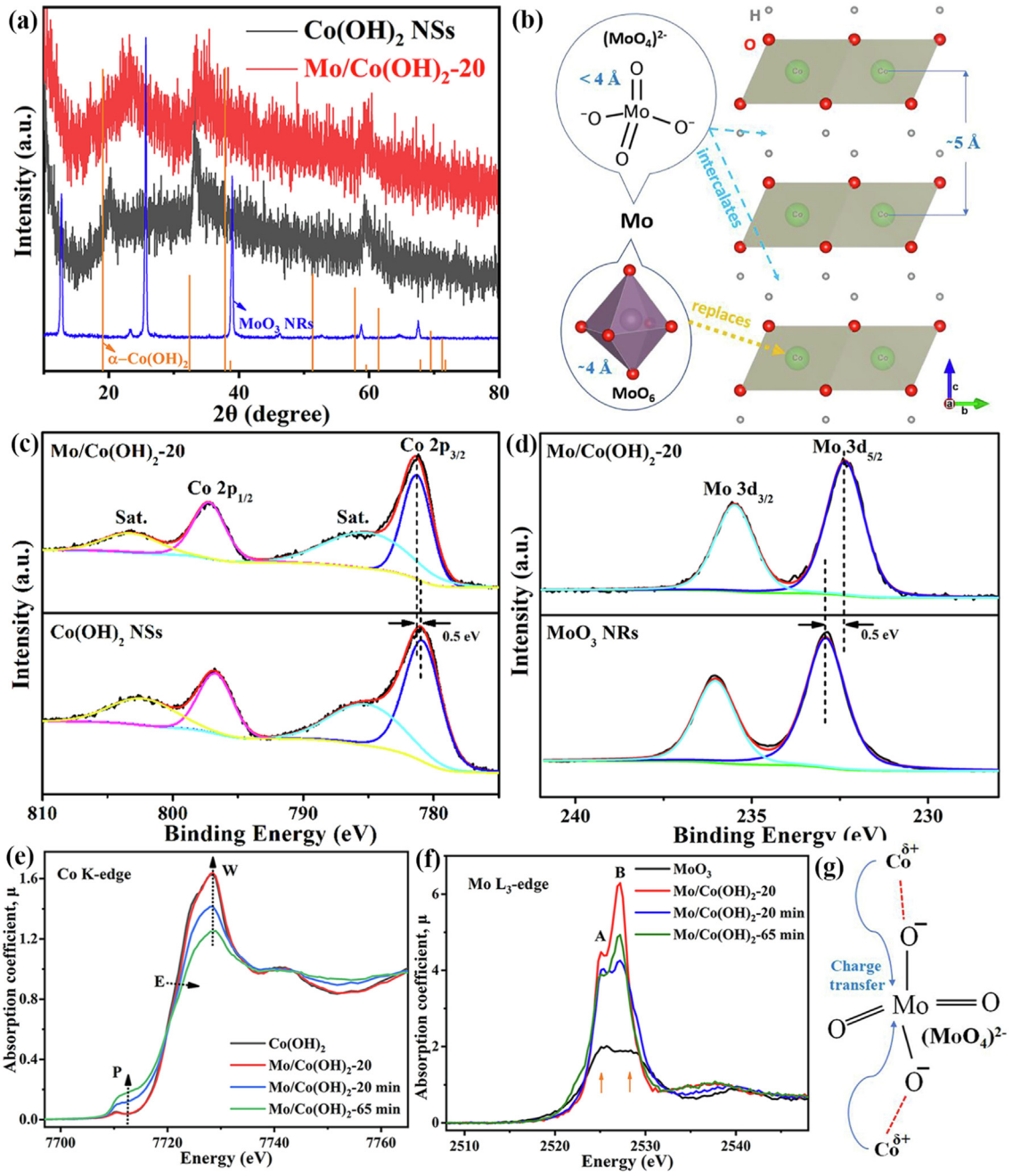

Fig. 3. (a) XRD patterns of Mo/Co(OH)$_2$-20 and Co(OH)$_2$ NSs along with MoO_3 nanorods and bulk α-Co(OH)$_2$. (b) Possible schematic mechanism of Mo doping in Co(OH)$_2$ NSs. (c) The high-resolution XPS Co 2p spectra of Mo/Co(OH)$_2$-20 and Co(OH)$_2$ NSs. (d) The high-resolution XPS Mo 3d spectra of Mo/Co(OH)$_2$-20 and MoO_3 NRs. Co K-edge (e) and Mo L-edge (f) XANES spectra for samples. (g) Proposed charge transfer schematic based on XRD, XPS and XAFS analysis.

troscopy (EDS) analysis (Fig. S12e) shows that the Mo/Co atomic ratio in the product is 1:11.6, which is close to the Mo/Co atomic ratio of Mo/Co(OH)$_2$-20. The test results in Fig. S13a show that the overpotential of MoO_3 NPs-Co(OH)$_2$ at a current density of 10 mA cm^{-2} is 320 mV, which is lower than that of Co(OH)$_2$ nanosheets, but higher than that of Mo/Co(OH)$_2$-20. This shows that doping with Mo is beneficial to improve the performance of Co(OH)$_2$. In addition, the optimization of the material structure will further enhance the catalyst activity. The Cdl of MoO_3 NPs-Co(OH)$_2$ is smaller than that of Mo/Co(OH)$_2$-20 (Fig. S13b and S13c), indicating that the electrochemical active area of the material is smaller than that of Mo/Co(OH)$_2$-20. This may be the reason for the poor performance of MoO_3 NPs-Co(OH)$_2$. Further, density functional theory (DFT, Fig. S14) proves that the Co(OH)$_2$ is a promising OER candidate. The insertion of molybdenum can improve the Co(OH)$_2$ activity through structure and electronic state regulation.

4. Conclusion

In summary, we obtained Mo-doped cobalt hydroxide nanosheet self-assembled hierarchical microtubules using MoO_3 nanorods as sacrificial templates. In 1 M KOH, the OER overpotential of Mo/Co(OH)$_2$ HMT at 10 mA cm^{-2} current density is only 288 mV, and its mass activity is 3.2 times higher than that of Co(OH)$_2$ nanosheets. Compared with previous studies, the introduction of molybdenum ions and the construction of nanosheet self-assembled microtubules exhibit great potential to enhance the

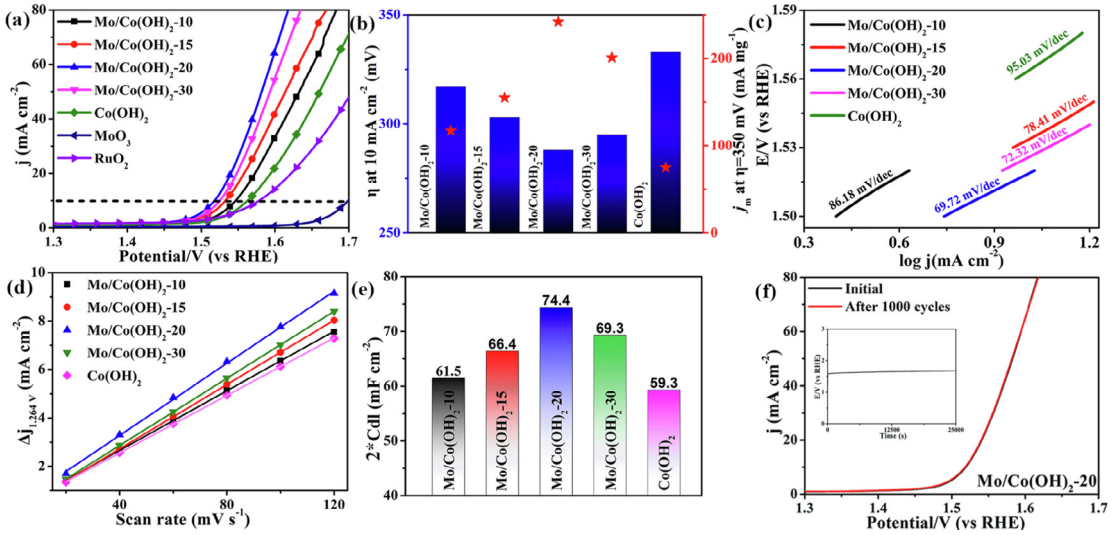

Fig. 4. (a) LSV curve of the samples. (b) The Overpotential of the samples at 10 mA cm^{-1}, and mass activity at 350 mV overpotential. (c) The Tafel curves of the samples. (d) The capacitance current (Δj) of the samples at 1.264 V (vs RHE) is plotted against the CV sweep speed. (e) 2Cdl values of the samples. (f) LSV curves for $Mo/Co(OH)_2$-20 at before and after CV cycles, the inset is the chronopotentiodynamic curve of $Mo/Co(OH)_2$-20 in 1.0 M KOH solution at a current density of 10 mA cm^{-2}.

OER catalytic performance of cobalt-based hydroxides (Table S3) [53–55, S1-S15] X-ray-based spectroscopic analysis determined that Mo(VI) with tetrahedral coordination intercalated in the interlayer of cobalt hydroxide, promoting interlayer separation. Meanwhile, Mo is connected to Co through oxygen bond, which promotes the transfer of Co charges to Mo and reduces the electron cloud density of Co ions. In addition, the self-assembled microtubule structure effectively separates the nanosheets and increases the accessible active area of the material. These are the key factors to improve the OER performance of materials. This study provides a scheme for the facile and rapid construction of hierarchical nanostructures for the synthesis of OER catalysts. In further work, in situ detection methods are needed to reveal the charge transfer process between Mo and Co ions and the formation and transition of intermediate products during OER catalysis.

CRediT authorship contribution statement

Chao Wang: Investigation, Data curation, Methodology, Writing – original draft. **Wen Li:** Investigation, Data curation, Methodology, Writing – original draft. **Andrey A. Kistanov:** Formal analysis, Methodology. **Harishchandra Singh:** Formal analysis, Methodology. **Yves Kayser:** Formal analysis, Methodology. **Wei Cao:** Formal analysis, Methodology. **Baoyou Geng:** Supervision, Writing – review & editing.

Data availability

Data will be made available on request.

Declaration of Competing Interest

The authors declare that they have no known competing financial interests or personal relationships that could have appeared to influence the work reported in this paper.

Acknowledgments

This work was supported by the National Natural Science Foundation of China (21871005, 22171005), the Program for Innovative Research Team of Anhui Education Committee, the Project for Collaborative Innovation of Anhui Higher Education Institutes (GXXT-2020-005, GXXT-2021-012, GXXT-2021-013). A.A.K. and W. C. acknowledge funding from the European Research Council (ERC) under the European Union's Horizon 2020 research and innovation program (grant agreement No. 101002219), and H.S. acknowledges financial supports from University of Oulu, Finland. The CSC–IT Center for Science, Finland is thanked for computational resources.

Appendix A. Supplementary data

Supplementary data to this article can be found online at https://doi.org/10.1016/j.jcis.2022.08.069.

References

[1] X.F. Li, Y.J. Liu, H.B. Chen, M. Yang, D.G. Yang, H.M. Li, Z.Q. Lin, Rechargeable Zn-Air Batteries with Outstanding Cycling Stability Enabled by Ultrafine FeNi Nanoparticles-Encapsulated N-Doped Carbon Nanosheets as a Bifunctional Electrocatalyst, Nano Lett 21 (7) (2021) 3098–3105.
[2] Y.F. Zhao, X. Zhang, X.D. Jia, G.I.N. Waterhouse, R. Shi, X.R. Zhang, F. Zhan, Y. Tao, L.Z. Wu, C.H. Tung, D. O'Hare, T.R. Zhang, Sub-3 nm Ultrafine Monolayer Layered Double Hydroxide Nanosheets for Electrochemical Water Oxidation, Adv. Energy Mater. 8 (18) (2018) 1703585.
[3] X. Zhang, Y.F. Zhao, Y.X. Zhao, R. Shi, G.I.N. Waterhouse, T.R. Zhang, A Simple Synthetic Strategy toward Defect-Rich Porous Monolayer NiFe-Layered Double Hydroxide Nanosheets for Efficient Electrocatalytic Water Oxidation, Adv. Energy Mater. 9 (24) (2019) 1900881.
[4] Y.P. Zhu, C.X. Guo, Y. Zheng, S.Z. Qiao, Surface and Interface Engineering of Noble-Metal-Free Electrocatalysts for Efficient Energy Conversion Processes, Acc. Chem. Res. 50 (4) (2017) 915–923.
[5] D. Liu, Q.Q. Lv, S.Q. Lu, J.J. Fang, Y.F. Zhang, X.D. Wang, Y.R. Xue, W. Zhu, Z.B. Zhuang, IrCuNi Deeply Concave Nanocubes as Highly Active Oxygen Evolution Reaction Electrocatalyst in Acid Electrolyte, Nano Lett. 21 (7) (2021) 2809–2816.
[6] Y. Lu, D.Q. Fan, Z.P. Chen, W.P. Xiao, C.C. Cao, X.F. Yang, Anchoring Co_3O_4 nanoparticles on MXene for efficient electrocatalytic oxygen evolution, Sci. Bull. 65 (6) (2020) 460–466.
[7] W.M. Li, C. Wang, X.F. Lu, Integrated transition metal and compounds with carbon nanomaterials for electrochemical water splitting, J. Mater. Chem. A 9 (7) (2021) 3786–3827.
[8] H.Y. Chang, Z.J. Liang, L. Wang, C. Wang, Research progress in improving the oxygen evolution reaction by adjusting the 3d electronic structure of transition metal catalysts, Nanoscale 14 (15) (2022) 5639–5656.
[9] Z.F. Huang, J.J. Song, Y.H. Du, S.B. Xi, S. Dou, J.M.V. Nsanzimana, C. Wang, Z.C.J. Xu, X. Wang, Chemical and structural origin of lattice oxygen oxidation in Co-Zn oxyhydroxide oxygen evolution electrocatalysts, Nat. Energy 4 (4) (2019) 329–338.
[10] A. Moysiadou, S. Lee, C.S. Hsu, H.M. Chen, X.L. Hu, Mechanism of Oxygen Evolution Catalyzed by Cobalt Oxyhydroxide: Cobalt Superoxide Species as a

Key Intermediate and Dioxygen Release as a Rate-Determining Step, J. Am. Chem. Soc. 142 (27) (2020) 11901–11914.
[11] Z.X. Li, X. Zhang, Y.K. Kang, C.C. Yu, Y.Y. Wen, M.L. Hu, D. Meng, W.Y. Song, Y. Yang, Interface Engineering of Co-LDH@MOF Heterojunction in Highly Stable and Efficient Oxygen Evolution Reaction, Adv. Sci. 8 (2) (2021) 2002631.
[12] Z.Y. Cai, X.M. Bu, P. Wang, J.C. Ho, J.H. Yang, X.Y. Wang, Recent advances in layered double hydroxide electrocatalysts for the oxygen evolution reaction, J. Mater. Chem. A 7 (10) (2019) 5069–5089.
[13] J. Yu, F. Yu, M.F. Yuen, C.D. Wang, Two-dimensional layered double hydroxides as a platform for electrocatalytic oxygen evolution, J. Mater. Chem. A 9 (15) (2021) 9389–9430.
[14] Y. Fang, Y.X. Liu, L. Qi, Y.R. Xue, Y.L. Li, 2D graphdiyne: an emerging carbon material, Chem. Soc. Rev. 51 (7) (2022) 2681–2709.
[15] P. Ding, H.Q. Song, J.W. Chang, S.Y. Lu, N-doped carbon dots coupled NiFe-LDH hybrids for robust electrocatalytic alkaline water and seawater oxidation, Nano Research, DOI: 10.1007/s12274-022-4377-4.
[16] Y.J. Tang, Y. Zou, D.D. Zhu, Efficient water oxidation using an Fe-doped nickel telluride-nickel phosphide electrocatalyst by partial phosphating, J. Mater. Chem. A 10 (23) (2022) 12438–12446.
[17] J. Hu, A. Al-Salihy, J. Wang, X. Li, Y.F. Fu, Z.H. Li, X.J. Han, B. Song, P. Xu, Improved Interface Charge Transfer and Redistribution in CuO-CoOOH p-n Heterojunction Nanoarray Electrocatalyst for Enhanced Oxygen Evolution Reaction, Adv. Sci. 8 (22) (2021) 2103314.
[18] S.M. Lin, Y. Yu, D.F. Sun, F.Y. Meng, W.H. Chu, L.Y. Huang, J. Ren, Q.M. Su, S.F. Ma, B.S. Xu, FeNi2P three-dimensional oriented nanosheet array bifunctional catalysts with better full water splitting performance than the full noble metal catalysts, J. Colloid Interf. Sci. 608 (2022) 2192–2202.
[19] L. Hui, Y.R. Xue, B.L. Huang, H.D. Yu, C. Zhang, D.Y. Zhang, D.Z. Jia, Y.J. Zhao, Y.J. Li, H.B. Liu, Y.L. Li, Overall water splitting by graphdiyne-exfoliated and -sandwiched layered double-hydroxide nanosheet arrays, Nat. Commun. 9 (2018) 5309.
[20] L.B. Wu, L. Yu, X. Xiao, F.H. Zhang, S.W. Song, S. Chen, Z.F. Ren, Recent Advances in Self-Supported Layered Double Hydroxides for Oxygen Evolution Reaction, Research-China 2020 (2020) 3976278.
[21] P.C. Wang, T. Jia, B.G. Wang, A critical review: 1D/2D nanostructured self-supported electrodes for electrochemical water splitting, J. Power Sources 474 (2020) 228621.
[22] B. Zhang, X.L. Zheng, O. Voznyy, R. Comin, M. Bajdich, M. Garcia-Melchor, L.L. Han, J.X. Xu, M. Liu, L.R. Zheng, F.P.G. de Arquer, C.T. Dinh, F.J. Fan, M.J. Yuan, E. Yassitepe, N. Chen, T. Regier, P.F. Liu, Y.H. Li, P. De Luna, A. Janmohamed, H.L.L. Xin, H.G. Yang, A. Vojvodic, E.H. Sargent, Homogeneously dispersed multimetal oxygen-evolving catalysts, Science 352 (6283) (2016) 333–337.
[23] W.J. Huang, J.M. Zhang, D.B. Liu, W.J. Xu, Y. Wang, J.D. Yao, H.T. Tan, K.N. Dinh, C. Wu, M. Kuang, W. Fang, R. Dangol, L. Song, K. Zhou, C.T. Liu, J.W. Xu, B. Liu, Q. Y. Yan, Tuning the Electronic Structures of Multimetal Oxide Nanoplates to Realize Favorable Adsorption Energies of Oxygenated Intermediates, ACS Nano 14 (12) (2020) 17640–17651.
[24] H. Mao, X. Guo, Y.L. Fu, H.R. Yang, Y. Zhang, R. Zhang, X.M. Song, Enhanced electrolytic oxygen evolution by the synergistic effects of trimetallic FeCoNi boride oxides immobilized on polypyrrole/reduced graphene oxide, J. Mater. Chem. A 8 (4) (2020) 1821–1828.
[25] Z. Zhai, W. Yan, J. Zhang, Layered FeCoNi double hydroxides with tailored surface electronic configurations induced by oxygen and unsaturated metal vacancies for boosting the overall water splitting process, Nanoscale 14 (11) (2022) 4156–4169.
[26] W.J. Sim, M.T. Nguyen, Z. Huang, S. Kheawhom, C. Wattanakit, T. Yonezawa, Efficient iron-cobalt oxide bifunctional electrode catalysts in rechargeable high current density zinc-air batteries, Nanoscale 14 (22) (2022) 8012–8022.
[27] Z.-Y. Pan, Z. Tang, Y.-Z. Zhan, D. Sun, Three-dimensional porous $CoNiO_2$@ reduced graphene oxide nanosheet arrays/nickel foam as a highly efficient bifunctional electrocatalyst for overall water splitting, Tungsten 2 (4) (2020) 390–402.
[28] M. Bajdich, M. Garcia-Mota, A. Vojvodic, J.K. Norskov, A.T. Bell, Theoretical Investigation of the Activity of Cobalt Oxides for the Electrochemical Oxidation of Water, J. Am. Chem. Soc. 135 (36) (2013) 13521–13530.
[29] B. Zhang, L. Wang, Z. Cao, S.M. Kozlov, F.P.G. de Arquer, C.T. Dinh, J. Li, Z.Y. Wang, X.L. Zheng, L.S. Zhang, Y.Z. Wen, O. Voznyy, R. Comin, P. De Luna, T. Regier, W.L. Bi, E.E. Alp, C.W. Pao, L.R. Zheng, Y.F. Hu, Y.J. Ji, Y.Y. Li, Y. Zhang, L. Cavallo, H.S. Peng, E.H. Sargent, High-valence metals improve oxygen evolution reaction performance by modulating 3dmetal oxidation cycle energetics, Nat. Catal. 3 (12) (2020) 985–992.
[30] P.F. Liu, S. Yang, L.R. Zheng, B. Zhang, H.G. Yang, Mo^{6+} activated multimetal oxygen-evolving catalysts, Chem. Sci. 8 (5) (2017) 3484–3488.
[31] S.M.N. Jeghan, J. Kim, G. Lee, Hierarchically designed CoMo marigold flower-like 3D nano-heterostructure as an efficient electrocatalyst for oxygen and hydrogen evolution reactions, Appl. Surf. Sci. 546 (2021) 149072.
[32] M. Krumrey, G. Ulm, High-accuracy detector calibration at the PTB four-crystal monochromator beamline, Nucl. Instrum. Meth. A 467 (2001) 1175–1178.
[33] B. Beckhoff, A. Gottwald, R. Klein, M. Krumrey, R. Muller, M. Richter, F. Scholze, R. Thornagel, G. Ulm, A quarter-century of metrology using synchrotron radiation by PTB in Berlin, Phys. Status Solidi B 246 (7) (2009) 1415–1434.
[34] J. Lubeck, B. Beckhoff, R. Fliegauf, I. Holfelder, P. Honicke, M. Muller, B. Pollakowski, F. Reinhardt, J. Weser, A novel instrument for quantitative nanoanalytics involving complementary X-ray methodologies, Rev. Sci. Instrum. 84 (4) (2013) 045106.
[35] F. Scholze, M. Procop, Modelling the response function of energy dispersive X-ray spectrometers with silicon detectors, X-Ray Spectrom. 38 (4) (2009) 312–321.
[36] R.H. Dong, H.R. Du, Y.X. Sun, K.F. Huang, W. Li, B.Y. Geng, Selective Reduction-Oxidation Strategy to the Conductivity-Enhancing Ag-Decorated Co-Based 2D Hydroxides as Efficient Electrocatalyst in Oxygen Evolution Reaction, Acs Sustain. Chem. Eng. 6 (10) (2018) 13420–13426.
[37] T.T. Jiang, X. Wang, J.H. Chen, Y.L. Mai, B. Liao, W. Hu, Hierarchical Ni/Co-LDHs catalyst for catalytic oxidation of indoor formaldehyde at ambient temperature, J. Mater .Sci.-Mater. El 31 (4) (2020) 3500–3509.
[38] L. Liu, J.P. Cheng, J. Zhang, F. Liu, X.B. Zhang, Effects of dodecyl sulfate and nitrate anions on the supercapacitive properties of alpha-Co(OH)(2), J. Alloy Compd. 615 (2014) 868–874.
[39] Y. Zhou, C. Wang, F. Chen, T. Wang, Y. Ni, H. Sun, N. Yu, B. Geng, Synchronous constructing ion channels and confined space of Co_3O_4 anode for high-performance lithium-ion batteries, Nano Res. (2022), https://doi.org/10.1007/s12274-022-4281-y.
[40] Y.N. Zhou, R.Y. Fan, Y.N. Cao, H.Y. Wang, B. Dong, H.Y. Zhao, F.L. Wang, J.F. Yu, Y. M. Chai, Oriented and robust anchoring of Fe via anodic interfacial coordination assembly on ultrathin Co hydroxides for efficient water oxidation, Nanoscale 13 (31) (2021) 13463–13472.
[41] K.B. Xu, J. Chao, W.Y. Li, Q. Liu, Z.J. Wang, X.J. Liu, R.J. Zou, J.Q. Hu, $CoMoO_4$ center dot $0.9H_2O$ nanorods grown on reduced graphene oxide as advanced electrochemical pseudocapacitor materials, Rsc Adv. 4 (65) (2014) 34307–34314.
[42] W.H. Zhang, Y.H. Tang, L.M. Yu, X.Y. Yu, Activating the alkaline hydrogen evolution performance of Mo-incorporated $Ni(OH)_2$ by plasma-induced heterostructure, Appl. Catal. B-Environ. 260 (2020) 118154.
[43] K. Inzani, M. Nematollahi, F. Vullum-Bruer, T. Grande, T.W. Reenaas, S.M. Selbach, Electronic properties of reduced molybdenum oxides, Phys. Chem. Chem. Phys. 19 (13) (2017) 9232–9245.
[44] A. Borgschulte, O. Sambalova, R. Delmelle, S. Jenatsch, R. Hany, F. Nuesch, Hydrogen reduction of molybdenum oxide at room temperature, Sci. Rep.-Uk 7 (2017) 40761.
[45] H. Singh, H. Ghosh, T.V.C. Rao, A.K. Sinha, P. Rajput, Observation of high-spin mixed oxidation state of cobalt in ceramic Co_3TeO_6, J. Appl. Phys. 116 (21) (2014) 214106.
[46] H. Singh, M. Topsakal, K. Attenkofer, T. Wolf, M. Leskes, Y.D. Duan, F. Wang, J. Vinson, D.Y. Lu, A.I. Frenkel, Identification of dopant site and its effect on electrochemical activity in Mn-doped lithium titanate, Phys. Rev. Mater. 2 (12) (2018) 125403.
[47] T. Yamamoto, Assignment of pre-edge peaks in K-edge x-ray absorption spectra of 3d transition metal compounds: electric dipole or quadrupole?, X-Ray Spectrom 37 (6) (2008) 572–584.
[48] G.M. Dalpian, Q.H. Liu, C.C. Stoumpos, A.P. Douvalis, M. Balasubramanian, M.G. Kanatzidis, A. Zunger, Changes in charge density vs changes in formal oxidation states: The case of Sn halide perovskites and their ordered vacancy analogues, Phys. Rev. Mater. 1 (2) (2017) 025401.
[49] A.P. Freitas, R.F. Andre, C. Poucin, T.K.C. Le, J. Imbao, B. Lassalle-Kaiser, S. Carenco, Guidelines for the Molybdenum Oxidation State and Geometry from X-ray Absorption Spectroscopy at the Mo L2,3-Edges, J. Phys. Chem. C 125 (32) (2021) 17761–17773.
[50] P.E.R. Blanchard, E. Reynolds, B.J. Kennedy, C.D. Ling, Z.M. Zhang, G. Thorogood, B.C.C. Cowie, L. Thomsen, An unconventional method for measuring the Tc L-3-edge of technetium compounds, J. Synchrotron. Radiat. 21 (2014) 1275–1281.
[51] Y.R. Xue, B.L. Huang, Y.P. Yi, Y. Guo, Z.C. Zuo, Y.J. Li, Z.Y. Jia, H.B. Liu, Y.L. Li, Anchoring zero valence single atoms of nickel and iron on graphdiyne for hydrogen evolution, Nat. Commun. 9 (2018) 1460.
[52] L. Hui, Y.R. Xue, H.D. Yu, Y.X. Liu, Y. Fang, C.Y. Xing, B.L. Huang, Y.L. Li, Highly Efficient and Selective Generation of Ammonia and Hydrogen on a Graphdiyne-Based Catalyst, J. Am. Chem. Soc. 141 (27) (2019) 10677–10683.
[53] G.L. Li, C. Liu, Z. Zhang, B.H. Cui, Y.A. Chen, Y.D. Deng, W.B. Hu, Nano-manufacturing of $Co(OH)_2$@NC for efficient oxygen evolution/reduction reactions, J. Mater. Sci. Technol. 81 (2021) 131–138.
[54] Y.P. Xiao, X. Chen, T.L. Li, Y.Y. Mao, C.L. Liu, Y.C. Chen, W.J. Wang, Mo-doped cobalt hydroxide nanosheets coupled with cobalt phosphide nanoarrays as bifunctional catalyst for efficient and high-stability overall water splitting, Int. J. Hydrogen Energy 47 (17) (2022) 9915–9924.
[55] Y.N. Zhou, R.Y. Fan, S.Y. Dou, B. Dong, Y. Ma, W.L. Yu, M.X. Li, Y.L. Zhou, C.G. Liu, Y.M. Chai, Tailoring electron transfer with Ce integration in ultrathin $Co(OH)_2$ nanosheets by fast microwave for oxygen evolution reaction, J. Energy Chem. 59 (2021) 299–305.